

Article

Influence of Oxide Coating Layers on the Stability of Gold Catalysts for Furfural Oxidative Esterification to Methyl Furoate

Juan Su ^{1,2}, Nannan Zhan ¹, Yuan Tan ^{1,*} , Xiangting Min ², Yan Xiao ^{1,2} and Botao Qiao ^{2,*}

¹ Hangzhou Institute of Advanced Studies, Zhejiang Normal University, Hangzhou 311231, China; sujuan@dicp.ac.cn (J.S.); nzhan@zjnu.edu.cn (N.Z.); xiaoyan@dicp.ac.cn (Y.X.)

² CAS Key Laboratory of Science and Technology on Applied Catalysis, Dalian Institute of Chemical Physics, Chinese Academy of Sciences, Dalian 116023, China; minxiangting@dicp.ac.cn

* Correspondence: yuantan2012@zjnu.edu.cn (Y.T.); bqiao@dicp.ac.cn (B.Q.);
Tel.: +86-571-82257902 (Y.T.); +86-411-84379416 (B.Q.)

Abstract: The use of gold nanoparticles (Au NPs) as catalysts has gained widespread attention in various reactions due to their high activity and selectivity under mild reaction conditions. However, one major challenge in utilizing these catalysts is their tendency to aggregate, leading to catalyst deactivation and hindering their amplification and industrial application. To overcome this issue, herein, we used a method by coating the surface of Au NPs with a thin layer of SiO₂, which resulted in the formation of a superior catalyst denoted as Au@SiO₂/ZA. Characterization studies revealed that the SiO₂ layer is coated on the surface of Au NPs and effectively prevents the aggregation and growth of the gold particles during the reaction process, which makes the catalyst display excellent stability in furfural (FF) oxidative esterification to methyl furoate (MF). Moreover, the stabilization strategy is not limited to SiO₂ alone. It can also be extended to other oxides such as ZrO₂, CeO₂, and TiO₂. We believe this work will provide a good reference for the design and development of an efficient and stable gold catalyst for the oxidative esterification reaction.

Keywords: gold catalyst; hydrotalcite; core-shell; furfural; oxidative esterification



Citation: Su, J.; Zhan, N.; Tan, Y.; Min, X.; Xiao, Y.; Qiao, B. Influence of Oxide Coating Layers on the Stability of Gold Catalysts for Furfural Oxidative Esterification to Methyl Furoate. *Catalysts* **2024**, *14*, 192. <https://doi.org/10.3390/catal14030192>

Academic Editor: Eric M. Gaigneaux

Received: 9 February 2024

Revised: 8 March 2024

Accepted: 10 March 2024

Published: 12 March 2024



Copyright: © 2024 by the authors. Licensee MDPI, Basel, Switzerland. This article is an open access article distributed under the terms and conditions of the Creative Commons Attribution (CC BY) license (<https://creativecommons.org/licenses/by/4.0/>).

1. Introduction

Due to the ever-increasing environmental concerns caused by our continuous consumption of fossil fuels, significant attention has been given to renewable resources like biomass [1–5]. Furfural (FF), bearing a natural furan ring and an active aldehyde group, has been recognized as a promising platform molecule derived from renewable biomass [6,7], which plays a crucial role in the production of pharmaceuticals, paints, plastics, pesticides, and various other industries [8,9]. Recently, intensive investigations have focused on the FF conversion due to its potential to undergo diverse transformations into furan derivatives under certain reaction conditions, including hydrogenation, oxidative esterification, oxidation condensation, ammonification, and so on [10–15].

One notable downstream product derived from FF is methyl 2-furoate (MF), which finds extensive applications in the fine chemical industry, including flavors, fragrances, extracting agents, and chemical intermediates [16–20]. The conventional approach for the industrial synthesis of MF involves esterification of 2-furoic acid (FA) with alcohols, where FF is initially oxidized to FA using potent stoichiometric oxidants like KMnO₄ [19,20]. However, this two-step method of producing MF is plagued by significant concerns regarding high costs, equipment corrosion, and environmental pollution [21,22]. Consequently, there is a strong imperative to develop efficient and sustainable processes for the direct transformation of FF to MF, typically utilizing environmentally friendly oxidants like O₂ or air [17].

Heterogeneous catalysts such as noble metal catalysts (i.e., Au [22–24], Pt [25], Pd [26], etc.) as well as transition metal catalysts (i.e., Co [27,28], etc.) have shown great potential

in the oxidative esterification process due to their capability of converting O₂ molecules into highly active atomic O or other reactive oxygen species [29]. This capability allows for the use of O₂ and air as green oxidants, avoiding the environmental damage and high cost associated with stoichiometric oxidants with toxicity. In particular, Au nanoparticles (NPs) have been extensively studied in various oxidative reactions, including low-temperature CO oxidation [30,31], aerobic oxidation of alcohols [32,33], and oxidative esterification of alcohols and aldehydes [22–24], due to their unique catalytic properties [34]. However, to ensure the effectiveness of Au NPs as catalysts, it is essential to control their particle sizes and prevent sintering and growth during the reaction process [35,36]. This can be achieved through controllable synthesis methods or by using stabilizing agents that prevent particle agglomeration [37,38].

The use of spatial confinement or physical coating strategies to confine Au NPs in an enclosed space can be an effective approach to obtaining stable gold catalysts [39–42]. Jiang et al. demonstrated this by encapsulating Au₂₅(Capt)₁₈ nanoclusters (NCs) into metal-organic frameworks (MOFs) and subsequently removing the surface ligand on the Au₂₅ NCs [39]. The fully exposed active sites of ligand-free Au₂₅ NCs protected by the MOFs resulted in a gold catalyst with enhanced activity and resistance to aggregation [39]. Wang et al. achieved a similar effect by encapsulating Au NPs within a porous TiO_x thin layer created by melamine in an oxidative environment [42]. The resulting TiO_x overlayer provided resistance to sintering, resulting in a gold catalyst that exhibited excellent reactivity and stability for CO oxidation [42]. In a more recent study, Zhang et al. developed a core-shell structured catalyst to mitigate the sintering susceptibility of Au NPs during calcination [31]. They coated the Au/TiO₂ surface with a SiO₂ shell, effectively suppressing the sintering of Au NPs even upon calcination at temperatures as high as 800 °C [31]. Overall, these examples demonstrate that the spatial confinement effect or physical coating strategies can be employed to enhance the stability and reactivity of gold catalysts by preventing agglomeration or sintering of the Au NPs.

In this study, we focus on developing oxide coatings on supported gold nanocatalysts for improved stability. The oxides used for coating include SiO₂, ZrO₂, CeO₂, and TiO₂. The probe reaction chosen to investigate the relationship between structure and activity is the oxidative esterification of FF. Previous research by Christensen et al. investigated the performance of a commercial Au/TiO₂ catalyst provided by the World Gold Council for FF oxidative esterification in the presence of a base, specifically 8% CH₃ONa [43]. However, the use of liquid bases led to issues such as increased energy consumption, leaching problems, and undesired side reactions [20,43]. To overcome these drawbacks, this study aims to design an alkali-free oxidation-esterification system. As we reported previously, Zn-Al hydrotalcite (ZA-HT) serves as a good precursor for the synthesis of a gold catalyst for the direct oxidative esterification of aldehydes to ester [44]. Therefore, in this work, a series of gold catalysts with different oxide coatings supported on ZA-HT were employed for the oxidative esterification of FF to synthesize MF. Various characterization techniques, including XRD, UV-vis, TEM, and XPS, were used to investigate the structural and electronic properties of the gold catalysts. The outcomes of this research are expected to contribute to the advancement of gold-catalyzed chemical processes, particularly those involving biorenewable feedstocks like FF.

2. Results and Discussion

2.1. Catalyst Preparation and Structure Characterization

Zn-Al hydrotalcite (ZA-HT)-supported Au catalysts coated with different amounts of SiO₂ were prepared via a two-step approach by altering the additive TEOS volumes (Figure 1a). Inductively coupled plasma optical emission spectroscopy (ICP-OES) analysis showed that the gold loadings in all catalysts were around 1 wt.% (Table 1). This indicates that the addition of SiO₂ did not significantly affect the gold loading. However, the Si loadings varied from 2.7 wt.% to 4.2 wt.% as the amount of TEOS increased, suggesting that the Si content in the catalysts can be controlled by adjusting the TEOS volume. N₂

physical adsorption-desorption measurements were conducted to investigate the effect of the SiO₂ coating on the catalysts' surface area and pore volumes. The results indicate that the addition of a small amount of SiO₂ results in much increased specific surface area (S_{BET}) and pore volumes (Figure 1b and Table 1), which most probably stemmed from the formation of some pore channels deriving from the micropore structure of SiO₂.

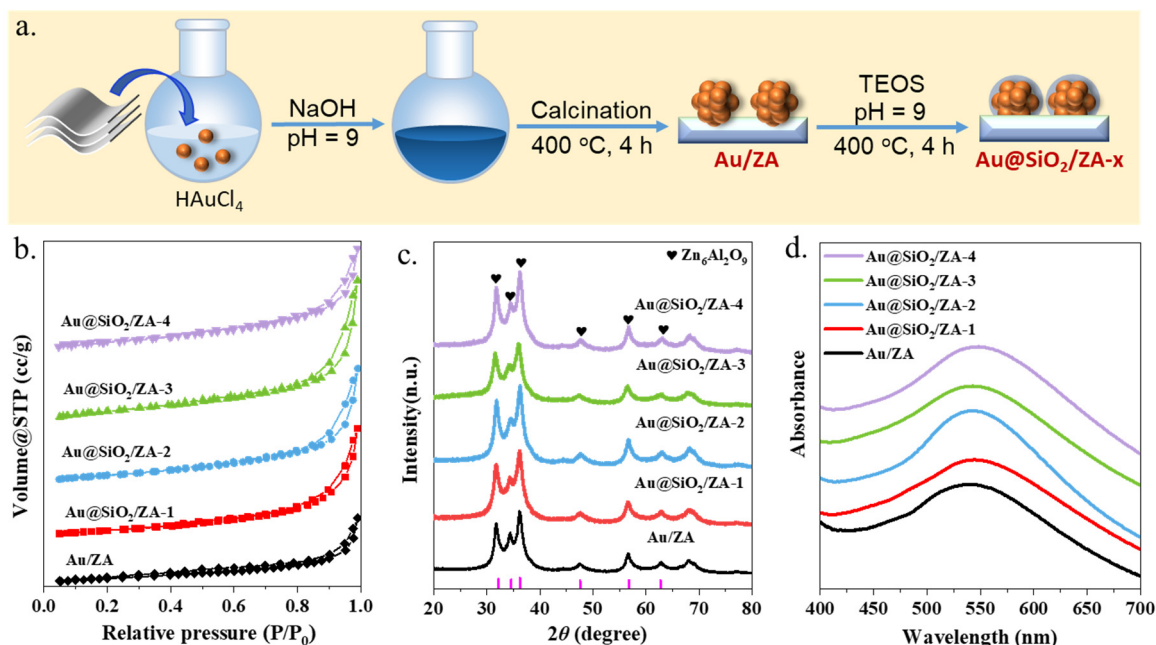


Figure 1. (a) The synthetic scheme of the gold-based catalysts with SiO₂ coatings. (b) N₂-physisorption isotherms; (c) XRD patterns; and (d) UV-vis spectra of the Au/ZTA and Au@SiO₂/ZA-X catalysts.

Table 1. Textural properties of supported Au catalysts with different contents of SiO₂ coatings.

Entry	Catalysts	Au Loadings (%) ^a	Si Loadings (%) ^a	S_{BET} (m ² /g) ^b	Total Volume (cm ³ /g) ^b	Pore Size (nm) ^b
1	Au/ZTA	1.2	-	89.3	0.23	3.8
2	Au@SiO ₂ /ZA-1	1.1	2.7	113.2	0.43	3.3
3	Au@SiO ₂ /ZA-2	1.1	3.1	118.2	0.48	3.3
4	Au@SiO ₂ /ZA-3	1.0	3.7	122.6	0.48	3.4
5	Au@SiO ₂ /ZA-4	1.1	4.2	117.3	0.36	3.8

^a Determined by ICP-OES; ^b Determined by N₂ physical absorption and desorption measurement.

The phase and lattice structure of the catalysts were examined by X-ray diffraction (XRD) (Figure 1c). The XRD patterns show sharp peaks located at 32.2°, 34.6°, 36.5°, 47.6°, 56.8°, and 62.7°, corresponding to the Zn₆Al₂O₉ phase (PDF No. 00-051-0037), which suggests that the calcined ZA-HT exists in the form of mixed metal oxides and that the Zn and Al atoms were evenly distributed in the catalysts' framework [45]. However, according to the Scherrer equation, the crystallinity decreased and disorder increased when SiO₂ was coated on the surface of Au/ZTA. The crystallite sizes of different samples were displayed in Table S1. This was likely due to the formation of amorphous SiO₂, consistent with the increased surface area. No diffraction peaks corresponding to Au were detected in any of the catalysts, indicating either the gold particles were very small or the amount of gold was below the detection limit of XRD. Ultraviolet-visible (UV-vis) spectra were used to examine the surface plasmonic resonance (SPR) band of the catalysts, which is related to the size of the gold particles (Figure 1d) [46]. The results showed similar absorption peaks at around 540 nm for all catalysts, suggesting similar particle sizes of gold in the samples [47].

Figure 2 depicts the high-resolution transmission electron microscopy (HRTEM) images of the Au/ZA and Au@SiO₂/ZA-X catalysts, where X represents the addition of different amounts of Si. It reveals the absence of large gold particles in all gold catalysts, with similar mean particle sizes in the range of 2~3 nm. This observation is consistent with the UV-vis and XRD results, indicating no significant alteration of the size of Au NPs due to the addition of Si. Further analysis of the HRTEM images reveals the presence of Au (111) with an interplanar crystal spacing of approximately 2.35 Å in all catalysts [24,48]. In addition, the lattice spacing of ~2.78 Å indicates the (010) plane of the Zn₆Al₂O₉, which closely contacts the gold species and acts as the supporting carrier to stabilize gold particles. Furthermore, a notable coating layer can be observed in the Si-containing samples when compared to Au/ZA. Elemental analysis of individual particles in the Au@SiO₂/ZA-4 sample by energy-dispersive X-ray (EDX)-mapping images indicates the co-presence of Au and Si in the same particle (Figure S1a,b). Line analysis of the EDX image on the basis of the composition profile signifies the successful synthesis of gold catalysts with SiO₂ coatings (Figure S1c,d).

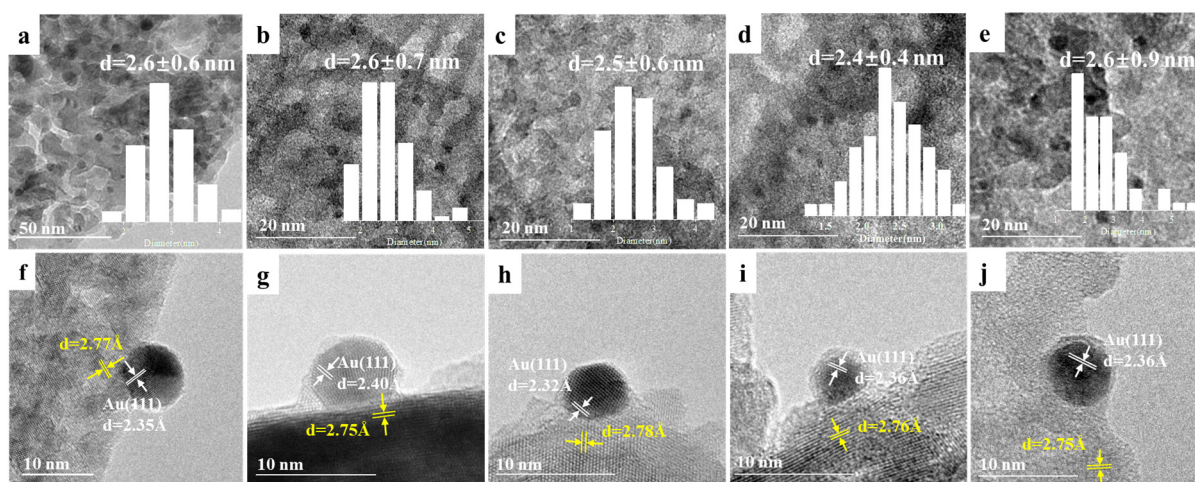


Figure 2. HRTEM images of (a,f) Au/ZA; (b,g) Au@SiO₂/ZA-1; (c,h) Au@SiO₂/ZA-2; (d,i) Au@SiO₂/ZA-3; and (e,j) Au@SiO₂/ZA-4 catalysts.

To further investigate the electronic structure of Au catalysts, high-resolution X-ray photoelectron spectroscopy (XPS) of Au 4f was conducted. In Figure 3, the binding energy (B.E.) of 83.3 eV and 87.0 eV can be assigned to Au 4f_{7/2} and Au 4f_{5/2}, respectively, indicating the presence of Au⁰ [44,49]. Notably, although the Au 4f_{5/2} band is overlapped by the Zn 3p XPS peak, which is positioned at 88.8 eV, the Au 4f_{7/2} band by deconvolution is also clear enough to distinguish the electronic state of Au. Moreover, the addition of SiO₂ did not obviously alter the electronic structure of the gold catalysts. As seen in Figure 3b–e, the B.E. of the Au 4f is maintained at a level of 83.1 eV, indicating the electron density around the Au atoms can be preserved. That is quite different from the previous report, in which more positively charged Au species will be present in the Si-containing samples [31]. We deduced that the different electronic structure might derive from the distinct synthesis method. Consequently, in combination with the results of TEM and EDX mapping, the SiO₂ in this work is speculated to be physically coated on the surface of gold.

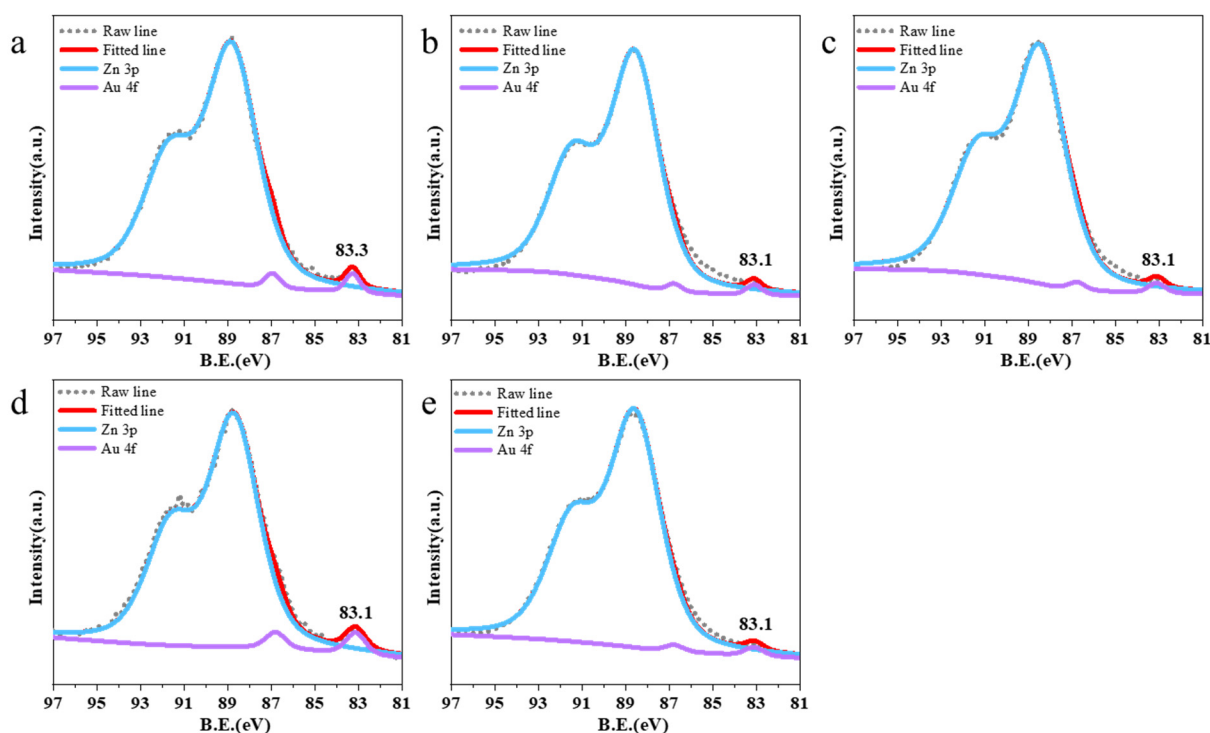


Figure 3. Au 4f XPS spectra of (a) Au/ZnO; (b) Au@SiO₂/ZnO-1; (c) Au@SiO₂/ZnO-2; (d) Au@SiO₂/ZnO-3; and (e) Au@SiO₂/ZnO-4.

2.2. Catalytic Performances of the above Catalysts for Oxidative Esterification of FF to MF

The catalytic performances of different supported gold catalysts for the oxidative esterification of FF to MF were tested in the batch-type stainless-steel autoclave, and the results are summarized in Table 2. As a control, the ZnO support was tested first (Table 2, entry 1), and no conversion was observed. On the other hand, Au/ZnO exhibited excellent performance: 94.2% FF conversion and 94.9% MF selectivity can be readily obtained within only 1 h (Table 2, entry 2), suggesting that gold plays a decisive role in the oxidative esterification process. The only by-product was acetal with a selectivity of 5.1%, which is formed by the hemiacetal condensation with methanol in the presence of specific catalysis sites or without catalysts [21]. The Au@SiO₂/ZnO-1 catalyst shows almost the same activity and selectivity as that of Au/ZnO, exhibiting FF conversion of 92.3% and MF selectivity of 95.0% (Table 2, entry 4) at the same reaction condition. The turnover frequency (TOF) values obtained in the kinetic control condition were also the same (232.2 and 231.4 h⁻¹) for Au/ZnO and Au@SiO₂/ZnO-1, respectively. However, increasing the Si content led to an obvious decrease in both activity and selectivity. For Au@SiO₂/ZnO-2, the conversion and selectivity decreased to 65.0% and 90.1%, respectively (Table 2, entry 6), giving rise to a TOF of 219.4 h⁻¹. Furthermore, Au@SiO₂/ZnO-3 (Table 2, entry 8) and Au@SiO₂/ZnO-4 (Table 2, entry 10) show even lower selectivity despite a similar conversion. Notably, for the Au@SiO₂/ZnO-4, the TOF is as low as 132.6 h⁻¹, only about half of that of the Au/ZnO and Au@SiO₂/ZnO-1. Increasing the reaction time from 1 h to 3 h resulted in FF conversion exceeding 90% for all catalysts (Table 2, entries 7, 9, and 11). However, prolonging the reaction time did not enhance the MF selectivity for Au@SiO₂/ZnO-4. This implies that the Si content greatly influences the catalytic performance of gold catalysts. As the particle size and valence state of Au are not significantly altered by the addition of Si, the difference might be due to its impact on the adsorption and activation capacity of reactant molecules such as O₂ and FF. Alfayate et al. previously reported that the Si incorporation into the Ti(III)APO-5 materials will influence the catalytic performances of the cyclohexene oxidation with hydrogen peroxide. They found that high Si content can

provide certain hydrophobicity to the material, which has an influence on the competitive adsorption of the polar hydrogen peroxide and the organic substrate [50].

Table 2. Catalytic performances of the sole support and different supported gold catalysts.

Entry	Catalysts	Conversion (%)	Selectivity (%)		TOF (h ⁻¹) ^b
			MF	DA	
1	ZA	0	0	0	
2	Au/ZA	94.2	94.9	5.1	232.2
3	Au/ZA ^a	99.9	98.9	1.1	
4	Au@SiO ₂ /ZA-1	92.3	95.0	5.0	231.4
5	Au@SiO ₂ /ZA-1 ^a	99.7	98.4	1.6	
6	Au@SiO ₂ /ZA-2	65.0	90.1	9.9	219.4
7	Au@SiO ₂ /ZA-2 ^a	94.1	92.2	7.8	
8	Au@SiO ₂ /ZA-3	62.2	75.4	24.6	218.0
9	Au@SiO ₂ /ZA-3 ^a	93.2	81.3	18.7	
10	Au@SiO ₂ /ZA-4	60.5	80.2	19.8	132.6
11	Au@SiO ₂ /ZA-4 ^a	90.3	79.7	20.3	

Reaction conditions: Cat. 0.1 g; FF: 75 μ L; CH₃OH: 5 mL; P_{O₂}: 0.6 MPa; T: 393 K; t: 1 h. ^a Reaction time: 3 h; ^b TOF is calculated by moles of converted FF per moles of gold per hour, with the conversion below 20%.

2.3. Dynamic Tests of Different Gold Catalysts for Oxidative Esterification

In order to further understand the factors affecting the reaction performance, dynamic tests were performed on the representative Au/ZA, Au@SiO₂/ZA-1, and Au@SiO₂/ZA-4 catalysts. Figure 4a presents the reaction rates in terms of O₂ pressure on the Au/ZA, Au@SiO₂/ZA-1, and Au@SiO₂/ZA-4 catalysts. It can be observed that the reaction order of O₂ over Au/ZA (0.27) closely resembled that of Au@SiO₂/ZA-1 (0.18) and Au@SiO₂/ZA-4 (0.20), indicating that the reaction rate is not very sensitive to O₂ pressure [21]. Figure 4b presents the reaction rates as a function of FF concentration. It can be seen that the reaction order of Au/ZA (0.50) and Au@SiO₂/ZA-1 (0.61) is much lower than that of Au@SiO₂/ZA-4 (1.10), implying that the reaction rate is highly relevant to the concentration of FF. That is, the contents of Si in the catalysts mainly affect the adsorption and activation of FF.

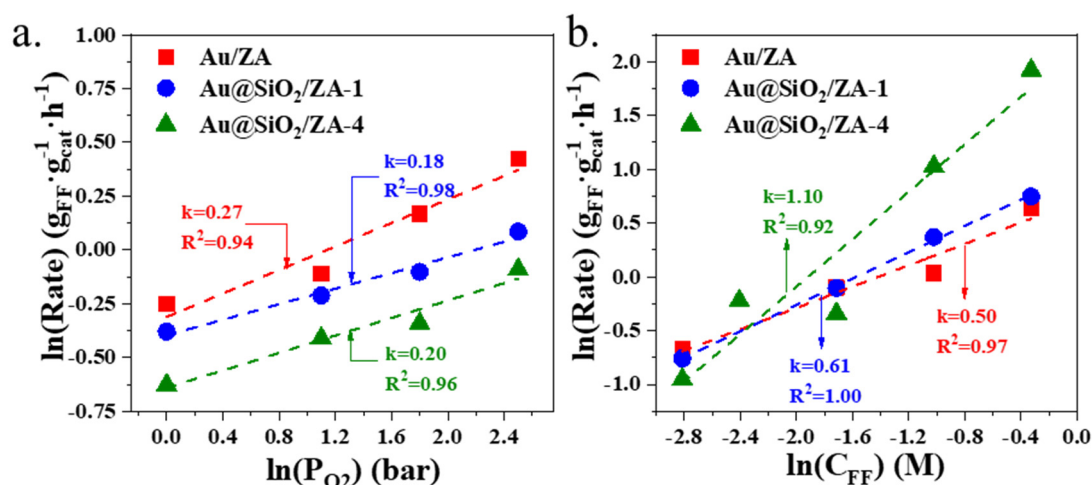


Figure 4. Dependence of the reaction rates on (a) the pressure of O₂ and (b) the concentration of FF over the Au/ZA, Au@SiO₂/ZA-1, and Au@SiO₂/ZA-4 catalysts.

2.4. Stability Tests of Gold Catalysts with or without SiO₂ Coating

Stability is generally considered one of the most important factors in evaluating the catalytic performance of a catalyst. Particularly, the stability of gold catalysts has often been regarded as a challenging problem in diverse reactions because Au NPs tend to sinter during reactions or upon high-temperature treatment [36,42]. In this regard, we aim to enhance the stability of the gold catalyst by encapsulating the Au NPs with SiO₂ layers. The recycle tests were conducted using the Au/ZA and Au@SiO₂/ZA-1 catalysts under identical reaction conditions (Figure 5). As expected, a noticeable decrease in FF conversion from 92.9% to 55.3% was observed for the Au/ZA catalyst, which is consistent with previous studies [22]. On the contrary, Au@SiO₂/ZA-1 exhibited excellent stability, with no detectable decrease in conversion in five recycle tests, suggesting that the SiO₂ coating layer indeed enhances the stability of Au.

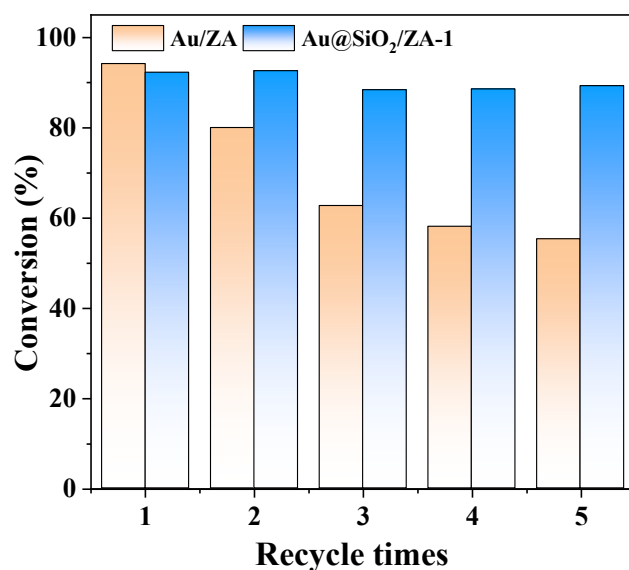


Figure 5. Recycling tests of Au/ZA and Au@SiO₂/ZA-1 catalysts for the oxidative esterification of FF to MF. Conditions: Cat. 0.1 g; FF: 75 μ L; CH₃OH: 5 mL; P_{O₂}: 0.6 MPa; T: 393 K; t: 1 h.

To clarify the origin of the improved stability of the SiO₂ coating layer for the Au catalysts, structural characterizations were carried out on the spent Au/ZA and Au@SiO₂/ZA-1 catalysts, respectively. In Figure 6a, it can be observed that both catalysts still exhibit a major phase of Zn₆Al₂O₉, similar to the fresh catalysts, indicating the phase structure of catalysts will not be changed over the reaction process. Nevertheless, the UV-vis spectra in Figure 6b reveal a significant wavenumber redshift in the plasmon resonance of gold over the Au/ZA catalyst, suggesting the probable agglomeration of gold nanoparticles over the Au/ZA catalyst [18]. To further confirm this, TEM characterization was also conducted on the spent Au/ZA and Au@SiO₂/ZA-1 catalysts. Compared with the fresh catalyst, the Au/ZA catalyst clearly shows a particle size increase from 2.6 nm (Figure 2a) to 5.0 nm (Figure 6c). Whereas the Au@SiO₂/ZA-1 catalyst demonstrates good stability after the reaction, with only a slight increase in particle size from 2.6 nm (Figure 2b) to 3.4 nm (Figure 6d). These findings strongly support the effectiveness of SiO₂ coating as a strategy for stabilizing gold particles and preventing their agglomeration in oxidative esterification.

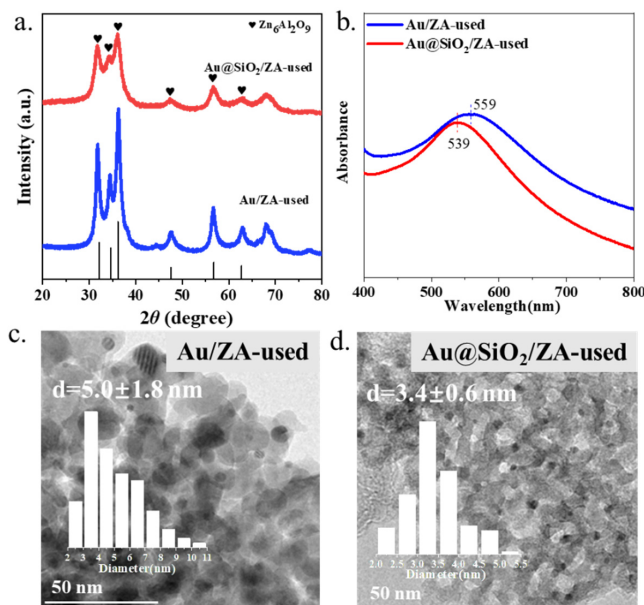


Figure 6. Characterizations of the spent Au/ZA and Au@SiO₂/ZA-1 catalysts: (a) XRD patterns; (b) UV-vis spectra; (c,d) TEM images and size distribution histograms.

2.5. Variation of Coating Layers with Other Oxides: ZrO₂, TiO₂, and CeO₂

To verify whether this coating strategy is applicable to other oxides to stabilize gold nanoparticles for FF oxidative esterification, a series of gold catalysts coated with ZrO₂, TiO₂, and CeO₂ were prepared according to the same method. As displayed in Figure 7, all catalysts, without optimization of coating oxide amount, show comparable good recycling stability in FF oxidation esterification when compared with the pristine Au/ZA catalyst (Figure 5). Moreover, it is evident that the catalytic performances differ significantly depending on the type of metal oxide coating on the gold surface. Among them, Au@ZrO₂/ZA shows the best performance with both high initial activity and selectivity (Figure 7a). After five cycles, the FF conversion over the Au@ZrO₂/ZA slightly decreased from 86.6% to 76.4%, with the selectivity of MF maintaining a high level above 98%. The Au@TiO₂/ZA catalyst (Figure 7b) shows inferior performance with initial FF conversion and MF selectivity of 74.8% and 98.7%, respectively. After five recycles, the FF conversion decreases to 68.5%, while the MF selectivity remains high at 95.7%. The Au@CeO₂/ZA catalyst (Figure 7c) exhibits lower initial activity when compared to Au@ZrO₂/ZA and Au@TiO₂/ZA, with FF conversion and MF selectivity of 46.9% and 95.2%, respectively. However, even after five reuses, the FF conversion only drops to 33.1%, and the MF selectivity is still maintained at 91%.

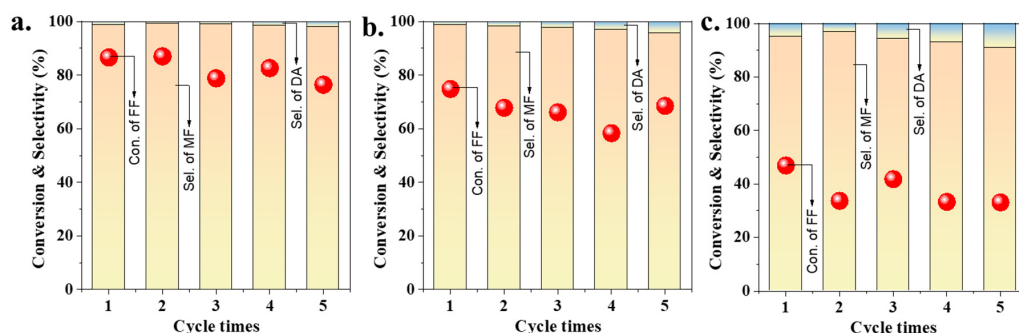


Figure 7. Recycling tests of (a) Au@ZrO₂/ZA; (b) Au@TiO₂/ZA; and (c) Au@CeO₂/ZA catalysts for the oxidative esterification of FF to MF. Conditions: Cat. 0.1 g; FF: 75 μ L; CH₃OH: 5 mL; P_{O₂}: 0.6 MPa; T: 393 K; t: 1 h.

The characterization results of the fresh and spent catalysts were displayed in Figures 8 and S2, and Table S1. From TEM images, the average particle sizes of gold over the fresh Au@ZrO₂/ZA, Au@TiO₂/ZA, and Au@CeO₂/ZA catalysts were 2.4 ± 0.4 nm (Figure 8a), 2.7 ± 0.7 nm (Figure 8b), and 3.1 ± 0.6 nm (Figure 8c). After recycling five times, the mean particle sizes of the spent catalysts slightly increased to 3.5 ± 0.7 nm (Figure 8d), 3.4 ± 0.7 nm (Figure 8e), and 3.3 ± 0.7 nm (Figure 8f), respectively. The XRD patterns of the spent catalysts are quite similar to those of the fresh catalysts, which shows the main phase of the ZA support (Figure S1a,c). No obvious sharp diffraction peaks of Au can be observed, indicating the presence of highly dispersed gold species. UV-vis spectra of the three catalysts suggest that the three catalysts show similar phase structure before and after catalytic tests, and the average particle sizes of gold just slightly increased as the plasma resonance peaks of Au became sharper (Figure S1b,d), which is in good line with the results of TEM. The results indicate that the encapsulation of Au nanoparticles with metal oxides, i.e., ZrO₂, TiO₂, and CeO₂, enhances the stability of the Au catalysts by preventing the aggregation of Au NPs. The situation is similar with SiO₂ oxides.

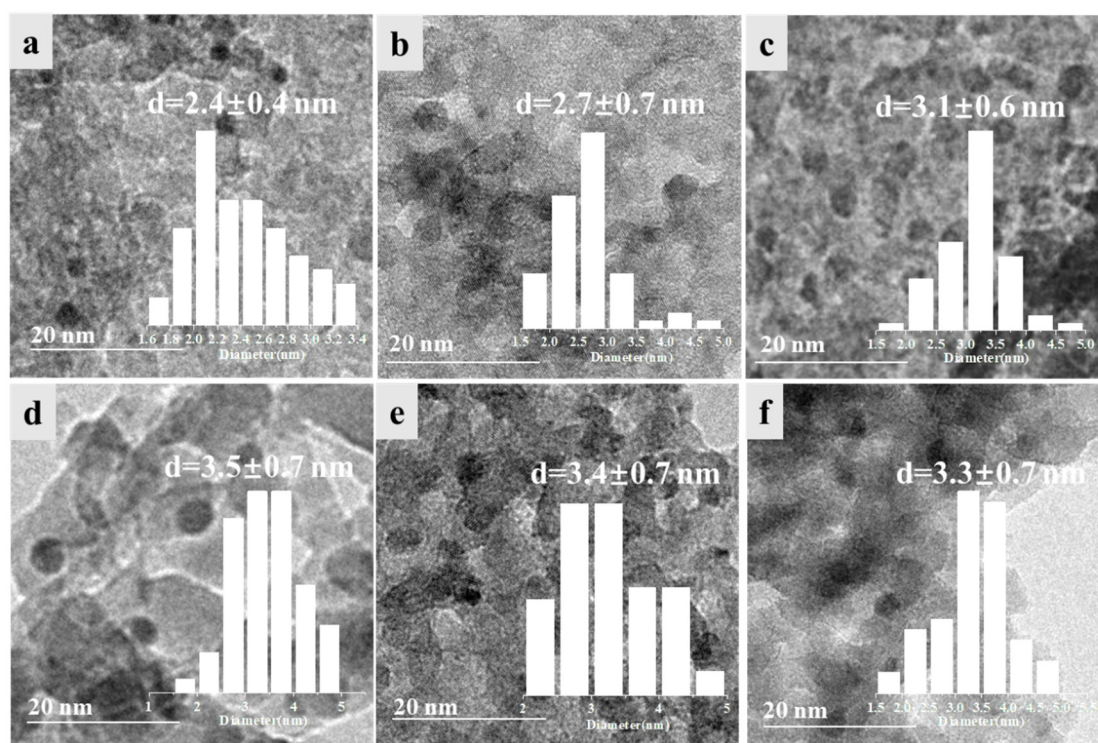


Figure 8. TEM images of the fresh and spent catalysts after recycling five times: (a,d) Au@ZrO₂/ZA; (b,e) Au@TiO₂/ZA; and (c,f) Au@CeO₂/ZA.

3. Materials and Methods

3.1. Chemicals

Chloroauric acid trihydrate (HAuCl₄·3H₂O, 99%, Au = 50%), titanium (IV) ethoxide (TiO₂, 33–35%), zirconium nitrate (Zr(NO₃)₄·5H₂O, 99.9%), furfural (FF, 99.0%), 1,2-xylene (99%), methyl 2-furoate (MF, 98%), and methanol (CH₃OH, 99.9%) were purchased from Anhui Zesheng Technology Co., Ltd. (Anqing, China). Zinc nitrate (Zn(NO₃)₂·6H₂O, 99.0%), cerium nitrate (Ce(NO₃)₂·6H₂O, 99.0%), and aluminum nitrate (Al(NO₃)₃·9H₂O, 99.0%) were purchased from Damao Chemical Reagent Factory. Sodium hydroxide (NaOH, 96.0%) was purchased from Tianda Chemical Reagent Co., Ltd. (Tianjin, China). Sodium carbonate anhydrous (Na₂CO₃, 99.8%) was purchased from Tianjin Guangfu Technology Development Co., Ltd. (Tianjin, China). Tetraethyl orthosilicate (TEOS, SiO₂ ≥ 28.4%) was purchased from Sinopharm Chemical Reagent Co., Ltd. (Shanghai, China).

3.2. Preparation of the Au/ZA Catalyst

ZnAl-Hydrotalcite (ZA-HT)-supported gold catalyst was prepared via the deposition-precipitation (DP) method. First of all, ZA-HT was synthesized by a co-precipitation method with a Zn/Al molar ratio of 3. In a typical synthesis procedure, $\text{Zn}(\text{NO}_3)_2 \cdot 6\text{H}_2\text{O}$ (0.21 mol) and $\text{Al}(\text{NO}_3)_3 \cdot 9\text{H}_2\text{O}$ (0.07 mol) were dissolved in deionized water (200 mL) to form solution A. NaOH (0.438 mol) and anhydrous Na_2CO_3 (0.113 mol) were dissolved in deionized water (200 mL) to form solution B. The two solutions, A and B, were mixed together with continuous stirring. Solution A was carefully added dropwise into solution B at a constant flow rate of $5.2 \text{ mL} \cdot \text{min}^{-1}$ at $80 \text{ }^\circ\text{C}$ in an oil bath. Subsequently, the resultant mixture was allowed to age for 20 h. The resulting suspension was then subjected to filtration to separate the solid from the liquid phase. Then the obtained solid was washed with deionized water and ethanol until pH reached ~ 7 . Finally, the product was dried overnight, resulting in the formation of the desired ZA-HT material. Secondly, HAuCl_4 ($20 \text{ g}_{\text{Au}}/\text{L}$, 0.5 mL) was added to the solution, along with 1 g of ZA-HT and 10 mL of deionized water. Subsequently, the pH of the solution was adjusted to 9 by a 0.2 M NaOH solution. The mixture was then stirred at RT for 12 h and shielded from light. The obtained product was thoroughly washed with deionized water, dried at $60 \text{ }^\circ\text{C}$ overnight, and calcined at $400 \text{ }^\circ\text{C}$ in a muffle furnace for 4 h with a heating rate of $5 \text{ }^\circ\text{C} \cdot \text{min}^{-1}$. The obtained catalyst was designated as Au/ZA.

3.3. Preparation of the Au Catalyst Coating with SiO_2 ($\text{Au}@\text{SiO}_2/\text{ZA-X}$)

ZA-HT supported Au catalysts coated with SiO_2 were prepared as follows: Firstly, 1 g of the previously obtained Au/ZA powders were dispersed into 50 mL of deionized water. Then specific volumes of TEOS were added to the catalyst suspension under vigorous stirring. The pH value was adjusted to ~ 9 by 0.2 M NaOH, and the solution was stirred at $70 \text{ }^\circ\text{C}$ for 3 h. Later, the catalysts were filtrated, washed, and dried overnight at $60 \text{ }^\circ\text{C}$ before calcining at $400 \text{ }^\circ\text{C}$ in a muffle furnace. The obtained samples were named $\text{Au}@\text{SiO}_2/\text{ZA-1}$, $\text{Au}@\text{SiO}_2/\text{ZA-2}$, $\text{Au}@\text{SiO}_2/\text{ZA-3}$, and $\text{Au}@\text{SiO}_2/\text{ZA-4}$, respectively, with TEOS volumes of 0.5 mL, 1 mL, 5 mL, and 15 mL.

3.4. Preparation of the Au Catalyst Coating with Other Metal Oxides ($\text{Au}@\text{MO}_2/\text{ZA}$)

The preparation of Au catalysts coated with other metal oxides was similar to that of the $\text{Au}@\text{SiO}_2/\text{ZA-X}$ sample. Firstly, 1 g of the Au/ZA powders was dispersed into 50 mL of deionized water, and then specific amounts of oxide precursors were added to the suspension under vigorous stirring. Then the solution was stirred at $70 \text{ }^\circ\text{C}$ for 3 h after the pH was regulated to ~ 9 . Lastly, the obtained product was washed, dried, calcined, and denoted as $\text{Au}@\text{ZrO}_2/\text{ZA}$, $\text{Au}@\text{CeO}_2/\text{ZA}$, and $\text{Au}@\text{TiO}_2/\text{ZA}$, respectively, with 0.3 g of zirconium nitrate, 280 μL of titanium ethoxide, and 0.2 g of cerium nitrate as the oxide precursors.

3.5. Catalytic Test

The oxidative esterification of furfural (FF) with methanol was judged in a batch-type stainless-steel autoclave (50 mL) with a magnetic stirrer and a heating device. Typically, 100 mg of catalyst powder was packed into the reactor, followed by adding a suspension containing 75 μL of FF, 55 μL of o-xylene, and 5 mL of methanol. Then the reactor was fed with O_2 and pressurized at 6 atm. The reaction temperature was enhanced to a specific value, and the reaction proceeded for a specific time. Afterwards, the reactor was put into an ice bath to stop the reaction, and the products were filtered out to conduct qualitative and quantitative analysis by gas chromatography (GC) (PAANA A91 pro, manufactured by Panna instruments Co., Ltd., Changzhou, China) equipped with a flame ionization detector (FID) and a HP-5 column ($30 \text{ m} \times 0.320 \text{ mm} \times 0.25 \text{ } \mu\text{m}$). In the stability test, the catalyst was recovered by centrifuging, washing with methanol, and calcining at $400 \text{ }^\circ\text{C}$ for 4 h.

The quantification of FF and its corresponding product (MF) was calculated with the calibration curves of the standard compounds. The quantification of by-products (DA) used

the same correction factor as MF. The concentrations of the compounds determined by GC were counted by the internal standard method. The conversion of FF, product selectivity, and carbon balance were calculated based on the following equations:

$$\text{Conversion}(\%) = \frac{\text{Moles of consumed FF}}{\text{Moles of initial FF}} \times 100\% \quad (1)$$

$$\text{Selectivity}(\%) = \frac{\text{Moles of product}}{\text{Moles of consumed FF}} \times 100\% \quad (2)$$

3.6. Characterizations

The actual contents of Au and Si in different catalysts were ascertained by using an inductively coupled plasma optical emission spectrometer (ICP-OES) 7300DV instrument (manufactured by PerkinElmer Co., Ltd., Waltham, MA, USA). After dissolving the sample in aqua regia, the solution was diluted to the specified concentration range for testing. UV–visible spectra were recorded on a Lambda950 instrument (manufactured by Perkin Elmer) with BaSO₄ as a reference and a wavelength range from 200 to 800 nm. X-ray diffraction (XRD) patterns were acquired by using a Zetium diffractometer (manufactured by Malvern Panalytical, Shanghai, China) fitted with a copper K α radiation source ($\lambda = 0.15432$ nm). The instrument was operated at 40 kV and 40 mA. Data collection was performed in continuous mode over the 2θ range of 5° to 90°. N₂-physisorption isotherms were tested on Quantachrome instruments at 77 K. The samples were outgassed at 300 °C for 3 h before the measurement. Corresponding experimental results were determined through the BET and BJH methods, enabling accurate calculations in this regard. X-ray photoelectron spectroscopy (XPS) was conducted on an X-ray photoelectron spectrometer (USA, ThermoFischer, Waltham, MA, USA, ESCALAB 250Xi) equipped with a monochromatized Al K α (1486.8 eV) and a non-monochromatized Mg K α excitation source (1253.6 eV). The spectroscopy was corrected with C as the standard (C 1s = 284.6 eV). High resolution transmission electron microscopy (HRTEM) measurements were recorded using a Tecnai G2 Spirit (FEI) microscope equipped with a JEOL 2100 electron microscope. The appropriate amounts of samples were prepared by dispersing the catalyst powder into ethanol for ultrasonic dispersion, then the suspension was dropwise added onto a microgrid mesh coated with carbon while waiting for the solvent to evaporate.

4. Conclusions

We have successfully prepared a SiO₂-coated Zn-Al hydrotalcite-supported Au NPs catalyst for the base-free oxidative esterification of FF to MF, which shows both high activity and excellent stability. The study indicated that the introduction of an appropriate amount of Si could maintain the good performance of gold NPs but effectively prevent the sintering of Au NPs during the reaction process, leading to a substantial improvement in the catalyst's stability. This finding highlights the importance of Si encapsulation in enhancing the durability of the catalyst. Moreover, the strategy used in this work seems universal and can be extended to other oxides as coating layers, such as ZrO₂, CeO₂, and TiO₂. This finding provides valuable insights into the development of stable and efficient gold catalysts for the base-free oxidative esterification reaction and helps to understand the catalytic behavior of gold catalysts for the production of FF and MF.

Supplementary Materials: The following are available online at <https://www.mdpi.com/article/10.3390/catal14030192/s1>. Figure S1: EDX-mapping and the line analysis of particles in the Au@SiO₂/ZA-4 catalyst; Figure S2: XRD patterns and UV–vis spectra of the supported Au catalysts with different oxide coatings before and after stability tests; Table S1: Characterizations of the supported Au catalysts with different oxide coatings; Table S2: Characterizations of the supported Au catalysts with different oxide coatings.

Author Contributions: Y.T. and B.Q. conceived the study; J.S. performed most of the experiments; N.Z. contributed with some of the characterizations; X.M. and Y.X. provided some valuable suggestions. All authors have read and agreed to the published version of the manuscript.

Funding: This research is supported by the National Natural Science Foundation of China (No. 22102149 and No. 21961142006).

Data Availability Statement: The data presented in this study are available on request from the corresponding author.

Acknowledgments: The authors appreciate the support from the public testing platform of Zhejiang Normal University and the Dalian Institute of Chemical Physics, Chinese Academy of Sciences.

Conflicts of Interest: The authors declare no conflicts of interest.

References

1. Dimitrakellis, P.; Delikonstantis, E.; Stefanidis, G.D.; Vlachos, D.G. Plasma technology for lignocellulosic biomass conversion toward an electrified biorefinery. *Green Chem.* **2022**, *24*, 2680–2721. [\[CrossRef\]](#)
2. Thanigaivel, S.; Vickram, S.; Manikandan, S.; Deena, S.R.; Subbaiya, R.; Karmegam, N.; Govarthan, M.; Kim, W. Sustainability and carbon neutralization trends in microalgae bioenergy production from wastewater treatment: A review. *Bioresour. Technol.* **2022**, *364*, 128057. [\[CrossRef\]](#) [\[PubMed\]](#)
3. Corma, A.; Iborra, S.; Velty, A. Chemical routes for the transformation of biomass into chemicals. *Chem. Rev.* **2007**, *107*, 2411–2502. [\[CrossRef\]](#)
4. He, L.; Chen, L.; Zheng, B.; Zhou, H.; Wang, H.; Li, H.; Zhang, H.; Xu, C.C.; Yang, S. Deep eutectic solvents for catalytic biodiesel production from liquid biomass and upgrading of solid biomass into 5-hydroxymethylfurfural. *Green Chem.* **2023**, *25*, 7410–7440. [\[CrossRef\]](#)
5. Li, C.; Zhao, X.; Wang, A.; Huber, G.W.; Zhang, T. Catalytic transformation of lignin for the production of chemicals and fuels. *Chem. Rev.* **2015**, *115*, 11559–11624. [\[CrossRef\]](#) [\[PubMed\]](#)
6. Lee, C.B.T.L.; Wu, T.Y. A review on solvent systems for furfural production from lignocellulosic biomass. *Renew. Sust. Energy Rev.* **2021**, *137*, 110172. [\[CrossRef\]](#)
7. Li, X.; Cong, L.; Lin, N.; Tang, C. Efficient electrochemical upgradation strategies for the biomass derivative furfural. *J. Mater. Chem. A* **2023**, *11*, 23133–23147. [\[CrossRef\]](#)
8. Wen, H.; Zhang, W.; Fan, Z.; Chen, Z. Recent Advances in Furfural Reduction via Electro-And Photocatalysis: From Mechanism to Catalyst Design. *ACS Catal.* **2023**, *13*, 15263–15289. [\[CrossRef\]](#)
9. Mariscal, R.; Maireles-Torres, P.; Ojeda, M.; Sádaba, I.; Granados, M.L. Furfural: A renewable and versatile platform molecule for the synthesis of chemicals and fuels. *Energy Environ. Sci.* **2016**, *9*, 1144–1189. [\[CrossRef\]](#)
10. Xue, Z.; Wu, S.; Fu, Y.; Luo, L.; Li, M.; Li, Z.; Shao, M.; Zheng, L.; Xu, M.; Duan, H. Efficient light-driven reductive amination of furfural to furfurylamine over ruthenium-cluster catalyst. *J. Energy Chem.* **2023**, *76*, 239–248. [\[CrossRef\]](#)
11. Wang, H.; Zhu, C.; Li, D.; Liu, Q.; Tan, J.; Wang, C.; Cai, C.; Ma, L. Recent advances in catalytic conversion of biomass to 5-hydroxymethylfurfural and 2, 5-dimethylfuran. *Renew. Sust. Energy Rev.* **2019**, *103*, 227–247. [\[CrossRef\]](#)
12. Long, J.; Xu, Y.; Zhao, W.; Li, H.; Yang, S. Heterogeneous catalytic upgrading of biofuranic aldehydes to alcohols. *Front. Chem.* **2019**, *7*, 529. [\[CrossRef\]](#) [\[PubMed\]](#)
13. Román, A.M.; Hasse, J.C.; Medlin, J.W.; Holewinski, A. Elucidating acidic electro-oxidation pathways of furfural on platinum. *ACS Catal.* **2019**, *9*, 10305–10316. [\[CrossRef\]](#)
14. Ayoub, N.; Toufaily, J.; Guénin, E.; Enderlin, G. Catalyst-free process for oxidation of furfural to maleic acid by high frequency ultrasonic activation. *Green Chem.* **2022**, *24*, 4164–4173. [\[CrossRef\]](#)
15. Ning, L.; Liao, S.; Liu, X.; Guo, P.; Zhang, Z.; Zhang, H.; Tong, X. A regulatable oxidative valorization of furfural with aliphatic alcohols catalyzed by functionalized metal-organic frameworks-supported Au nanoparticles. *J. Catal.* **2018**, *364*, 1–13. [\[CrossRef\]](#)
16. Ferraz, C.P.; Braga, A.H.; Ghazzal, M.N.; Zieliński, M.; Pietrowski, M.; Itabaiana, I., Jr.; Dumeignil, F.; Rossi, L.M.; Wojcieszak, R. Efficient oxidative esterification of furfural using Au nanoparticles supported on group 2 alkaline earth metal oxides. *Catalysts* **2020**, *10*, 430. [\[CrossRef\]](#)
17. Tong, X.; Liu, Z.; Yu, L.; Li, Y. A tunable process: Catalytic transformation of renewable furfural with aliphatic alcohols in the presence of molecular oxygen. *Chem. Commun.* **2015**, *51*, 3674. [\[CrossRef\]](#) [\[PubMed\]](#)
18. Delparish, A.; Bouter, A.W.N.d.L.D.; Yercan, A.; van der Schaaf, J.; D'Angelo, M.F.N. Bringing the promises of microreactors and gold catalysis to lignocellulosic biomass valorization: A study on oxidative transformation of furfural. *Chem. Eng. J.* **2023**, *452*, 138903. [\[CrossRef\]](#)
19. Manzoli, M.; Menegazzo, F.; Signoretto, M.; Marchese, D. Biomass derived chemicals: Furfural oxidative esterification to methyl-2-furoate over gold catalysts. *Catalysts* **2016**, *6*, 107. [\[CrossRef\]](#)
20. Escobar, A.; Pérez, M.; Sathicq, A.; García, M.; Paola, A.; Romanelli, G.; Blustein, G. Alkyl 2-furoates obtained by green chemistry procedures as suitable new antifoulants for marine protective coatings. *J. Coat. Technol. Res.* **2018**, *16*, 159–166. [\[CrossRef\]](#)

21. Huo, N.; Ma, H.; Wang, X.; Wang, T.; Wang, G.; Wang, T.; Hou, L.; Gao, J.; Xu, J. High-efficiency oxidative esterification of furfural to methylfuroate with a non-precious metal Co-NC/MgO catalyst. *J. Catal.* **2017**, *38*, 1148–1154.
22. Radhakrishnan, R.; Thiripuranthagan, S.; Devarajan, A.; Kumaravel, S.; Erusappan, E.; Kannan, K. Oxidative esterification of furfural by Au nanoparticles supported CMK-3 mesoporous catalysts. *Appl. Catal. A* **2017**, *545*, 33–43. [[CrossRef](#)]
23. Cho, A.; Byun, S.; Cho, J.H.; Kim, B.M. AuPd-Fe₃O₄ Nanoparticle-Catalyzed Synthesis of Furan-2,5-dimethylcarboxylate from 5-Hydroxymethylfurfural under Mild Conditions. *ChemSusChem* **2019**, *12*, 2310–2317. [[CrossRef](#)] [[PubMed](#)]
24. Li, J.; Li, H.; Liu, Z.; Akri, M.; Tan, Y.; Kang, L.; Chi, J.; Qiao, B.; Ding, Y. Synergic effect between gold and vanadate substituted hydroxyapatite support for synthesis of methyl methacrylate by one-step oxidative esterification. *Chem. Eng. J.* **2022**, *431*, 133207. [[CrossRef](#)]
25. Zhao, X.; Fang, R.; Shen, Z.; Wang, F.; Li, Y. Atomic decoration of Pt on Co nanoparticles for enhanced oxidative esterification performances. *AIChE J.* **2023**, e18340. [[CrossRef](#)]
26. Li, F.; Li, X.-L.; Li, C.; Shi, J.; Fu, Y. Aerobic oxidative esterification of 5-hydroxymethylfurfural to dimethyl furan-2,5-dicarboxylate by using homogeneous and heterogeneous PdCoBi/C catalysts under atmospheric oxygen. *Green Chem.* **2018**, *20*, 3050–3058. [[CrossRef](#)]
27. Wang, R.; Lu, K.; Zhang, J.; Li, X.; Zheng, Z. Regulation of the Co-N_x Active Sites of MOF-Templated Co@NC Catalysts via Au Doping for Boosting Oxidative Esterification of Alcohols. *ACS Catal.* **2022**, *12*, 14290–14303. [[CrossRef](#)]
28. Jiang, B.-L.; Lin, Y.; Wang, M.-L.; Liu, D.-S.; Xu, B.-H.; Zhang, S.-J. Cobalt-catalyzed direct transformation of aldehydes to esters: The crucial role of an enone as a mediator. *Org. Chem. Front.* **2019**, *6*, 801–807. [[CrossRef](#)]
29. Song, F.; Cen, S.; Wan, C.; Wang, L. Nano-Au Anchored in Organic Base Group-Grafted Silica Aerogel: A Durable and Robust Catalysts for Green Oxidative Esterification of Furfural. *ChemCatChem* **2022**, *14*, e202200704. [[CrossRef](#)]
30. Yang, N.; Pattison, S.; Douthwaite, M.; Zeng, G.; Zhang, H.; Ma, J.; Hutchings, G.J. Influence of Stabilizers on the Performance of Au/TiO₂ Catalysts for CO Oxidation. *ACS Catal.* **2021**, *11*, 11607–11615. [[CrossRef](#)]
31. Zhang, Y.; Zhang, J.; Zhang, B.; Si, R.; Han, B.; Hong, F.; Niu, Y.; Sun, L.; Li, L.; Qiao, B.; et al. Boosting the catalysis of gold by O₂ activation at Au-SiO₂ interface. *Nat. Commun.* **2020**, *11*, 558. [[CrossRef](#)] [[PubMed](#)]
32. Wu, G.; Zhao, G.; Sun, J.; Cao, X.; He, Y.; Feng, J.; Li, D. The effect of oxygen vacancies in ZnO at an Au/ZnO interface on its catalytic selective oxidation of glycerol. *J. Catal.* **2019**, *377*, 271–282. [[CrossRef](#)]
33. Zhou, Y.; Wang, Z.; Ye, B.; Huang, X.; Deng, H. Ligand effect over gold nanocatalysts towards enhanced gas-phase oxidation of alcohols. *J. Catal.* **2021**, *400*, 274–282. [[CrossRef](#)]
34. Hammer, B.; Norskov, J.K. Why gold is the noblest of all the metals. *Nature* **1995**, *376*, 238–240. [[CrossRef](#)]
35. Turner, M.; Golovko, V.B.; Vaughan, O.P.H.; Abdulkin, P.; Berenguer-Murcia, A.; Tikhov, M.S.; Johnson, B.F.G.; Lambert, R.M. Selective oxidation with dioxygen by gold nanoparticle catalysts derived from 55-atom clusters. *Nature* **2008**, *454*, 981–983. [[CrossRef](#)]
36. Du, X.; Huang, Y.; Pan, X.; Han, B.; Su, Y.; Jiang, Q.; Li, M.; Tang, H.; Li, G.; Qiao, B. Size-dependent strong metal-support interaction in TiO₂ supported Au nanocatalysts. *Nat. Commun.* **2020**, *11*, 5811. [[CrossRef](#)] [[PubMed](#)]
37. Higaki, T.; Li, Y.; Zhao, S.; Li, Q.; Li, S.; Du, X.; Yang, S.; Chai, J.; Jin, R. Atomically Tailored Gold Nanoclusters for Catalytic Application. *Angew. Chem.* **2019**, *131*, 8377–8388. [[CrossRef](#)]
38. Pei, Y.; Wang, P.; Ma, Z.; Xiong, L. Growth-Rule-Guided Structural Exploration of Thiolate-Protected Gold Nanoclusters. *Acc. Chem. Res.* **2019**, *52*, 23–33. [[CrossRef](#)]
39. Wang, H.; Liu, X.; Yang, W.; Mao, G.; Meng, Z.; Wu, Z.; Jiang, H.L. Surface-Clean Au₂₅ Nanoclusters in Modulated Microenvironment Enabled by Metal–Organic Frameworks for Enhanced Catalysis. *J. Am. Chem. Soc.* **2022**, *144*, 22008–22017. [[CrossRef](#)]
40. Zhong, Y.; Liao, P.; Kang, J.; Liu, Q.; Wang, S.; Li, S.; Liu, X.; Li, G. Locking Effect in Metal@MOF with Superior Stability for Highly Chemoselective Catalysis. *J. Am. Chem. Soc.* **2023**, *145*, 4659–4666. [[CrossRef](#)]
41. Wu, K.; Wang, X.Y.; Guo, L.L.; Xu, Y.J.; Zhou, L.; Lyu, Z.Y.; Liu, K.Y.; Si, R.; Zhang, Y.W.; Sun, L.D.; et al. Facile synthesis of Au embedded CuO_x-CeO₂ core/shell nanospheres as highly reactive and sinter-resistant catalysts for catalytic hydrogenation of p-nitrophenol. *Nano Res.* **2020**, *13*, 2044–2055. [[CrossRef](#)]
42. Liu, S.; Xu, W.; Niu, Y.; Zhang, B.; Zheng, L.; Liu, W.; Li, L.; Wang, J. Ultrastable Au nanoparticles on titania through an encapsulation strategy under oxidative atmosphere. *Nat. Commun.* **2019**, *10*, 5790. [[CrossRef](#)]
43. Taarning, E.; Nielsen, I.S.; Egeblad, K.; Madsen, R.; Christensen, C.H. Chemicals from renewables: Aerobic oxidation of furfural and hydroxymethylfurfural over gold catalysts. *ChemSusChem* **2008**, *1*, 75–78. [[CrossRef](#)] [[PubMed](#)]
44. Li, H.; Tan, Y.; Chen, X.; Yang, W.; Huang, C.; Li, J.; Ding, Y. Efficient synthesis of methyl methacrylate by one step oxidative esterification over Zn-Al-mixed oxides supported gold nanocatalysts. *Catalysts* **2021**, *11*, 162. [[CrossRef](#)]
45. Ortiz, G.R.; Lartundo-Rojas, L.; Samaniego-Benítez, J.E.; Jiménez-Flores, Y.; Calderón, H.; Mantilla, A. Photocatalytic behavior for the phenol degradation of ZnAl layered double hydroxide functionalized with SDS. *J. Environ. Manag.* **2021**, *277*, 111399. [[CrossRef](#)] [[PubMed](#)]
46. Chen, D.; Shi, J.; Shen, H. High-dispersed catalysts of core-shell structured Au@SiO₂ for formaldehyde catalytic oxidation. *Chem. Eng. J.* **2020**, *385*, 123887. [[CrossRef](#)]
47. Hernández-Ramírez, E.; Wanga, J.A.; Chena, L.F.; Valenzuela, M.A.; Dalaib, A.K. Development of CeO₂-and TiO₂-Based Au Nanocatalysts for Catalytic Applications. *Appl. Surf. Sci.* **2016**, *399*, 77–85.

48. Tan, Y.; Liu, X.Y.; Zhang, L.; Wang, A.; Li, L.; Pan, X.; Miao, S.; Haruta, M.; Wei, H.; Wang, H.; et al. *Angew. Chem. Int. Ed.* **2017**, *56*, 2709–2713. [[CrossRef](#)]
49. Liu, Z.; Tan, Y.; Li, J.; Li, X.; Xiao, Y.; Su, J.; Chen, X.; Qiao, B.; Ding, Y. Ag substituted Au clusters supported on Mg-Al-hydrotalcite for highly efficient base-free aerobic oxidation of 5-hydroxymethylfurfural to 2,5-furandicarboxylic acid. *Green Chem.* **2022**, *24*, 8840–8852. [[CrossRef](#)]
50. Alfayate, A.; Sepúlveda, R.; Sánchez-Sánchez, M.; Pérez-Pariente, J. Influence of Si Incorporation into the Novel Ti(III)APO-5 Catalysts on the Oxidation of Cyclohexene in Liquid Phase. *Top. Catal.* **2016**, *59*, 326–336. [[CrossRef](#)]

Disclaimer/Publisher’s Note: The statements, opinions and data contained in all publications are solely those of the individual author(s) and contributor(s) and not of MDPI and/or the editor(s). MDPI and/or the editor(s) disclaim responsibility for any injury to people or property resulting from any ideas, methods, instructions or products referred to in the content.